DFT + U investigation of magnetocrystalline anisotropy of Mn-doped transition-metal dichalcogenide monolayers

Adlen Smiri
Faculté des Sciences de Bizerte, Laboratoire de Physique des Matériaux: Structure et Propriétés, Université de Carthage, 7021 Jarzouna, Tunisia and LPCNO, Université Fédérale de Toulouse Midi-Pyrénées and INSA, Centre National de la Recherche Scientifique, UPS, 135 Avenue de Rangueil, 31077 Toulouse, France

Sihem Jaziri
Faculté des Sciences de Bizerte, Laboratoire de Physique des Matériaux: Structure et Propriétés, Université de Carthage, 7021 Jarzouna, Tunisia and Faculté des Sciences de Tunis, Laboratoire de Physique de la Matiére Condensée and Département de Physique, Université Tunis el Manar, Campus Universitaire, 2092 Tunis, Tunisia

Samir Lounis
Peter Grünberg Institut and Institute for Advanced Simulation, Forschungszentrum Jülich and JARA, 52425 Jülich, Germany and Faculty of Physics, University of Duisburg-Essen and CENIDE, 47053 Duisburg, Germany

Iann C. Gerber*
LPCNO, Université Fédérale de Toulouse Midi-Pyrénées and INSA, Centre National de la Recherche Scientifique, UPS, 135 Avenue de Rangueil, 31077 Toulouse, France

(Received 4 March 2021; accepted 16 April 2021; published 3 May 2021)

Doped transition-metal dichalcogenide monolayers exhibit exciting magnetic properties for the benefit of two-dimensional spintronic devices. Using density functional theory (DFT) incorporating Hubbard-type correction (DFT + U) to account for the electronic correlation, we study the magnetocrystalline anisotropy energy (MAE) characterizing Mn-doped MS_2 (M = Mo, W) monolayers. A single isolated Mn dopant exhibits a large perpendicular magnetic anisotropy of 35 meV (8 meV) in the case of Mn-doped WS_2 (MoS_2) monolayer. This value originates from the Mn in-plane orbitals degeneracy lifting due to the spin-orbit coupling. In pairwise doping, the magnetization easy axis changes to the in-plane direction with a weak MAE compared to single Mn doping. Our results suggest that diluted Mn-doped MS_2 monolayers, where the Mn dopants are well separated, could potentially be a candidate for the realization of ultimate nanomagnet units for future magnetic storage applications.

DOI: 10.1103/PhysRevMaterials.5.054001

I. INTRODUCTION

Inducing magnetism in nonmagnetic semiconductor atomically thin monolayers (MLs) is a current field of investigation in material science to reach applications in storage and quantum spin processing. Interestingly, very few experimental works on doping MoS_2 MLs with other transition metals [1,2] are available, while most of the reported studies are theoretical ones [3–9]. It has been shown that doping can induce strong ferromagnetism [2–6,8–12] and large magnetic anisotropy that corresponds to direction-dependent magnetism [7,13–16] in two-dimensional (2D) materials. MoS_2 ML appears to be an emblematic case in the family of transition-metal dichalcogenide semiconductors (TMDs) since it possesses peculiar physical properties [17–21]. It is characterized by robust excitonic binding energies of hundreds of meV, which suggests several potential applications such as laser or light-emitting diodes fields [1,22–24]. Furthermore, MoS_2 ML has specific transport properties [25–30]. In particular, this 2D semiconductor has high low-temperature electron mobility (up to 1000 cm^2/V s) [25–28] and low-power dissipation [27,29,30] which makes it a good candidate to build transistors [27,29–31]. Thus inducing magnetism in this type of well-featured materials is of first importance to address spintronic applications [1,2,4,5,9]. The substitution of Mo atoms in 2H-MoS_2 ML by Mn ones is one way to realize promising magnetic 2D-TMDs candidates [1,2,4,5,9]. From a thermodynamical point of view, exchanging Mn at Mo sites is found energetically favorable under the S-rich regime [9]. Moreover, it has been shown that Mn dopant clustering within MoS_2 ML appears to be a more stable configuration than the well-dispersed Mn dopant case [8]. Experimentally, doped Mn-MoS_2 ML samples have been realized either by using vapor phase de-

*igerber@insa-toulouse.fr

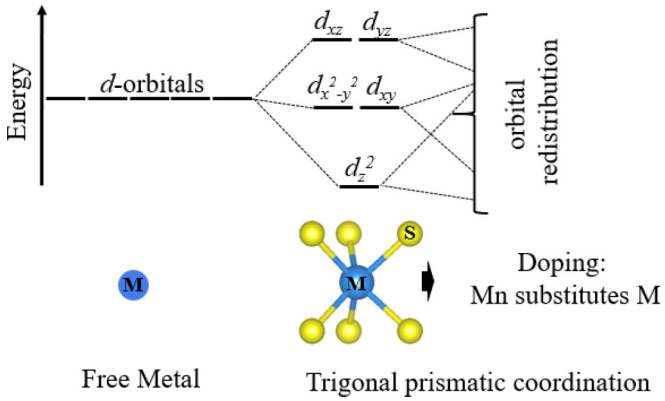

FIG. 1. Schematic diagram explaining the M (M = Mo or W) d orbitals splitting under a crystal field of the trigonal prismatic symmetry. The d orbitals of the isolated M atom (left) split into three categories (middle) for MS_2 MLs. The d orbitals are expected to show, locally, further splitting when the Mn dopant takes the place of the M atom.

position techniques for low doping concentration [17], or by a hydrothermal method to reach higher doping concentration [2]. Theoretical studies have shown that doping MoS_2 ML with Mn promotes a strong ferromagnetism with high Curie temperatures [1,2,4,5,9].

In addition to the desired goal of high Curie temperature in 2D-TMDs, it is highly desirable to have a large magnetic anisotropy energy (MAE), which defines the energy barrier preserving the magnetic moments in a preferential direction against thermal fluctuations at room temperature [32–34]. In order to achieve high-density magnetic data storage devices, the magnetic anisotropy induced by single adatoms or single atoms is of great interest [7,16,35–37]. For substitutional Mn-doped MoS_2 ML, to our knowledge most of the studies focused on the ferromagnetism aspect without addressing its MAE. The only works dealing with MAE estimates in doped TMDs have considered (i) magnetic adatoms (Mn or Fe) on MoS_2 ML containing S divacancies [7] which reach MAE values of a few meVs with a preferential in-plane magnetization for Mn adatoms as in [38] and a preferential out-of-plane magnetization for a single adsorbed Fe and (ii) the doping of WS_2 ML by substitutional Co and Fe atoms that can achieve large perpendicular magnetic anisotropy of a few tenths of a meV [16].

It is well known that in pristine 2H-MS_2 ML (with M=Mo, W), under a trigonal prismatic coordination, the d-M orbitals are split in three categories [39,40] in the associated point group D_{3h} (Fig. 1). The M lowest-energy orbital corresponds to d_{z^2} which reflects its weak coupling with the surrounding atoms. The M intermediate-energy orbitals d_{xy} and $d_{x^2-y^2}$ are coupled to each other, when the highest-energy orbitals d_{xz} and d_{yz} are strongly coupled with the $3p$ S atom. As a consequence, those orbitals dominate the conduction- and valence-band edges characters in MS_2 ML [40–42], and are the origin of strong spin-orbit coupling (SOC) in the valence band [43,44] in the K point of the Brillouin zone, up to 426 and 150 meV for WS_2 and MoS_2 MLs, respectively. Any substitution of a M atom by a dopant, such as a Mn atom, should lead to a local orbital redistribution with respect to the energy due to crystal-field effects [3,4,9], with spin splitting. The dopant orbital magnetic moment direction is thus settled by both SOC and the crystal-field effect, possibly inducing MAE [43,45]. Understanding and possibly tuning the MAE of Mn-doped MS_2 ML appear crucial to prospect the potential of these materials in information storage devices.

In this paper, density functional theory (DFT) corrected by a Hubbard term (DFT + U) to account for strong electronic correlation in $3d$ orbitals is considered to study the possible magnetic anisotropy in the Mn-doped MS_2 ML systems. The importance of such correlations was previously recognized in bulk $3d$ Ni and Fe atoms, where their account led to MAEs with a better agreement with experiments [46,47], since these effects can trigger large orbital magnetic moments [46]. Another possibility as in Ref. [39], would be to use hybrid functionals, to provide a better localization of the $3d$ orbitals, as proposed to obtain reliable spin-orbit splitting of defect states at the origin of the MAE. However, the computational cost associated to this task remains too large. Hence, taking into account the U dependence, as done in the present paper, is necessary to establish a complete study of the magnetic anisotropy of Mn-MS_2-doped MLs.

Using DFT + U method, we have estimated and compared the MAE in single and pairwise Mn-doped MS_2 MLs. In particular, we have first investigated the MAE induced by a single isolated Mn dopant, representative of a moderate dopant's concentration around 4%. Then, in view of the preferential clustering of substitutional Mn atoms in MS_2 ML, we have studied the MAE's sensitivity to the separation distance between Mn atoms. To this end, various configurations have been constructed by placing two Mn atoms in M sites of a zigzag or/and armchair patterns with different Mn-Mn separations. In addition, for relevant doping cases, through the analysis of dopant SOC we have investigated and rationalized the MAE's origin.

II. METHODS AND COMPUTATIONAL DETAILS

Spin-polarized DFT as implemented in Vienna *ab initio* simulation package (VASP) was used in this paper [48,49]. The core potential was approximated by the projected augmented wave (PAW) scheme [50,51]. Perdew-Burke-Ernzerhof formulation of the generalized gradient approximation was applied to describe the exchange-correlation interaction [52]. In addition, a Hubbard U correction [53] was adopted in order to better describe the localization of $3d$ Mn orbitals. The criterion of atom force convergence, used for all structure relaxations, was fixed to 0.02 eV/Å, with an energy cutoff of 400 eV for plane waves and 950 eV for the cutoff energy of the augmentation charges' plane-wave representation. In order to model the geometry of Mn-doped MS_2 MLs, supercells of size $5 \times 5 \times 1$ and $7 \times 7 \times 1$ were considered, with a 20-Å-thick vacuum region to separate adjacent MLs. The initialized lattice parameters are equal to 3.18 Å for WS_2 ML and 3.20 Å for MoS_2 ML. To calculate the MAE, a $4 \times 4 \times 1$, $7 \times 7 \times 1$, and $9 \times 9 \times 1$ Γ-centered Monkhorst-Pack grid with the tetrahedron smearing method of Blöchl [54] were tested to obtain accurate results. For density of state calculations, the k-points grid has been increased to $12 \times 12 \times 1$

and the smearing method was switched to the Gaussian type with 0.02-eV width.

The magnetic anisotropy energy of Mn-doped MS_2 is determined by performing a fully self-consistent SOC and noncollinear calculations with different orientations of the magnetic moments of Mn impurities. In particular, we calculate the total energies E_x and E_z when the magnetization direction is parallel to x and z axis, respectively. Therefore, the MAE is given by

$$\mathrm{MAE} = E_x - E_z, \tag{1}$$

where x, y, z represent the crystalline axes with the z axis perpendicular to the ML plane. Positive MAE stands for preferential out-of-plane magnetization corresponding to perpendicular magnetic anisotropy (PMA), while negative MAE stands for a preferential in-plane magnetization which is known as in-plane magnetic anisotropy (IMA). Furthermore, in order to elucidate the origin of MAE, spin-orbit energy is calculated, using a scalar relativistic approximation [55] as implemented in VASP code [56], through the following expression:

$$E_{\mathrm{SOC}} = \left\langle \frac{\hbar^2}{2m^2c^2}\frac{1}{r}\frac{dV(r)}{dr}\hat{\boldsymbol{L}}.\hat{\boldsymbol{S}} \right\rangle. \tag{2}$$

Here, $\hat{\boldsymbol{L}}$ and $\hat{\boldsymbol{S}}$ denote the orbital and spin angular momentum operators, respectively, when $V(r)$ is the spherical part of the effective potential within the PAW sphere.

III. RESULTS AND DISCUSSION

A. Magnetic anisotropy of an isolated Mn atom in MoS_2 ML

1. U dependence of magnetic anisotropy

To study the electronic correlation effects on the magnetic anisotropy of Mn-MS_2-doped MLs, the calculated MAEs with respect to U parameter are shown in Fig. 2(a). Note here that for each Hubbard term U, the geometrical optimization is repeated. In the absence of the correlation correction, the easy axis of magnetization is oriented along x which indicates an IMA for the two systems. Here, the MAE value of Mn-WS_2-doped ML is in good agreement with that of Refs. [16,38]. We find that without U, the magnitudes of MAEs are almost the same for both investigated systems. However, by introducing the correlation effects, a change in the magnetization easy axis occurs at $U = 2$ eV resulting in energetically favored PMA states, with MAEs much larger for Mn-WS_2 ML than for Mn-MoS_2 ML. A similar change of MAE sign under U-parameter variation was found for Fe and Ni atoms [46]. We note that Mn-WS_2 ML MAE is larger than the Mn-MoS_2 ML one.

In particular, for $U > 1$ eV, Mn-MoS_2-doped ML exhibits a large MAE of 8 meV compared to the results of Cong *et al.* [7], where the largest MAE value was found to be 1.3 meV for the Mn adatom implanted in a disulfur vacancy in MoS_2 ML. Higher MAEs are found in the case of Mn-WS_2-doped ML for the same range of U. Indeed, the MAE reaches 30, 35, and 24 meV for the Hubbard parameter of 2, 3, and 4 eV, respectively. A thermal stability at room temperature of the magnetic anisotropy can be envisaged in the case of Mn-doped-WS_2 ML.

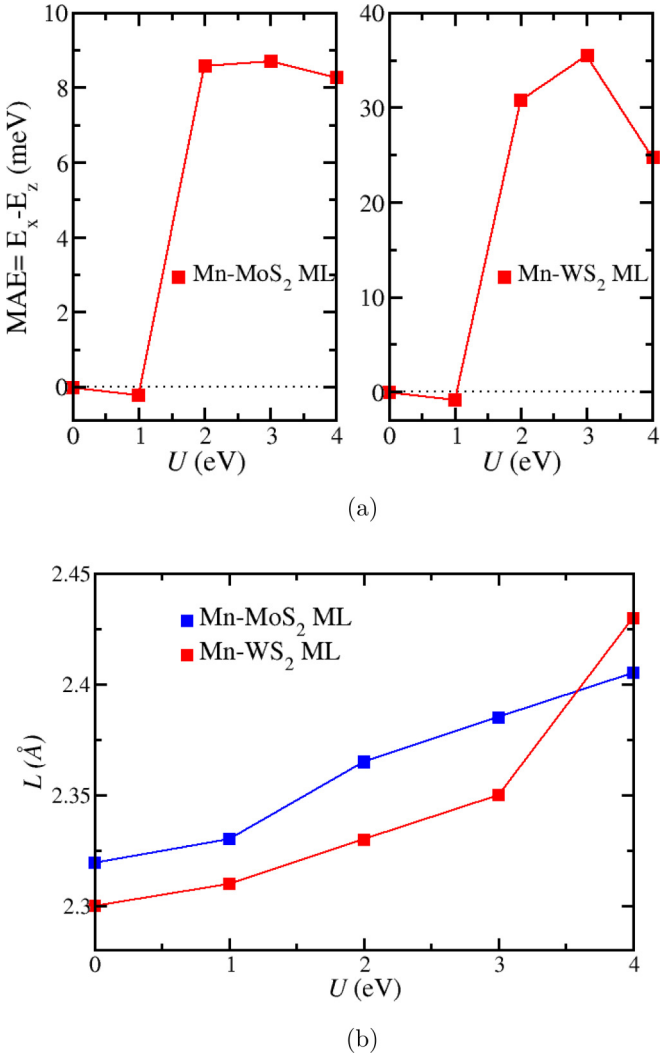

FIG. 2. (a) The magnetic anisotropy energy (MAE) of Mn-MS_2-doped MLs as a function of the Hubbard parameter U. (b) The length L of the bonds formed between Mn dopant and the first nearest-neighboring S host atoms as a function of U.

2. Influence of crystal structure on the magnetic anisotropy

Owing to the Hubbard U parameter, the equilibrium atomic positions can vary and thus impact the electronic structures. Hence, a connection between the MAE variation and the structural modifications, both under U parameter, is possible. To reveal the effect of correlations on the local crystal structure, the S-Mn bond length (L) is plotted in Fig. 2(b) as a function of U parameter upon geometry optimization. Interestingly when U is increased, L becomes larger too. In the meantime, the on-site Coulomb correlation enhances the magnetic anisotropy magnitude. The enhancement of MAE seems to be correlated to the increase in the S-Mn bond lengths suggesting a common electronic origin. In terms of electronic structure, the L increase results in a decrease of the overlapping between $3p$ S and $3d$ Mn orbitals. To explore the orbital distribution and hybridization in Mn-doped MS_2 MLs, the projected density of states (pDOS) for DFT and DFT + U are shown in Fig. 3. From DFT, the $3d$ Mn orbital energy

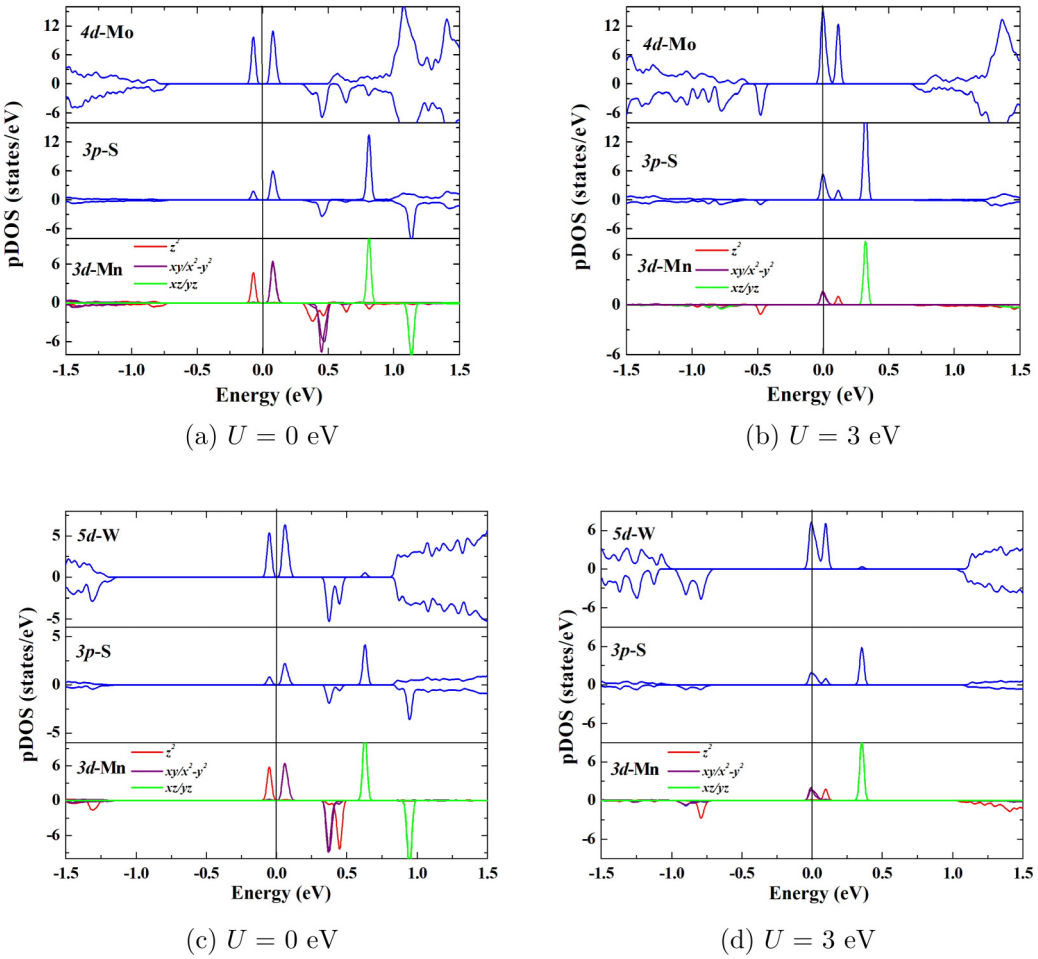

FIG. 3. The DFT (a), (c) and the DFT + U (b, d) (for $U = 3$ eV) pDOS of 3d states of Mn dopant and d and 4p states of its neighboring M and S atoms, respectively.

level splits into three different levels under crystal-field effect of the trigonal prismatic coordination: a twofold degenerate level containing the out-of-plane orbitals (d_{xz}, d_{yz}) with the highest energies among 3d Mn levels and a twofold degenerate level containing the in-plane orbitals (d_{xy}, $d_{x^2-y^2}$) with intermediate energies and a nondegenerate level containing the perpendicular orbital (d_{z^2}) with the lowest energies. The d_{xz} and d_{yz} degenerate level has the highest energy because they are oriented toward the chalcogen atoms as indicated in Fig. 1. Hence, d_{xz} and d_{yz} orbitals have a greater overlapping with 3p S orbitals than the rest of the Mn orbitals that are lower in energy. Interestingly, once the correlation effect is included, d_{xz} and d_{yz} degenerate level starts to shift toward lower energies, which explains the increase of the S-Mn bond lengths.

Furthermore, the decrease of the hybridization, under U variation, occurs for all Mn 3d orbitals and not only d_{xz} and d_{yz} orbitals. The Mn orbitals (d_{xy}, $d_{x^2-y^2}$) and d_{z^2} mainly hybridize with the d orbitals of the metal M (see Fig. 3). For $U \in [0;3]$ for M=W and $U \in [0;4]$ for M=Mo [Fig. 5(b)], the in-plane d_{xy} and $d_{x^2-y^2}$ degenerate level slightly shifts in energy until they cross the Fermi level and exceed the spin-up d_{z^2} level. In the meantime, a spin-down d_{z^2} state appears close to the valence band which maintains the same energetic order of 3d orbitals.

To further elucidate the MAE connection with local modifications of the geometries, we recalculate the MAE with a fixed lattice parameter of about 3.2 Å obtained upon a DFT geometry optimization (case II) for MoS_2 ML. The results are plotted in Fig. 4 and compared to the ones obtained after complete lattice parameter optimization for each U as already discussed (case I). When comparing the MAEs variations with U of cases I and II, the major differences appear at $U = 2$ eV for both systems and at $U = 4$ eV for Mn-WS_2 ML. In particular, the MAEs of case I show larger (smaller) values at $U = 2$ (4) eV with respect to MAEs of case II for MoS_2 (WS_2) MLs. Therefore, the dependence of the crystal structure on U can potentially be critical in determining the MAE based on the value of U itself.

We try now to elucidate the electronic origin of the changes and similarities between MAEs obtained in cases I and II with or without geometry optimizations. In particular, for each U parameter, the DOS is represented for U-dependent and -independent crystal structures in Fig. 5. For $U < 2$ eV, the DOS of case I and II show comparable features which explain the coincidence between the corresponding MAEs. In particular, the Fermi level lays between the d_{z^2} and $d_{xy}/d_{x^2-y^2}$ orbitals. For $U = 2$ eV, the latter electronic properties are obtained in case II, whereas the Fermi level crosses the spin-up bands of the twofold degenerated $d_{xy}/d_{x^2-y^2}$ orbitals in case I.

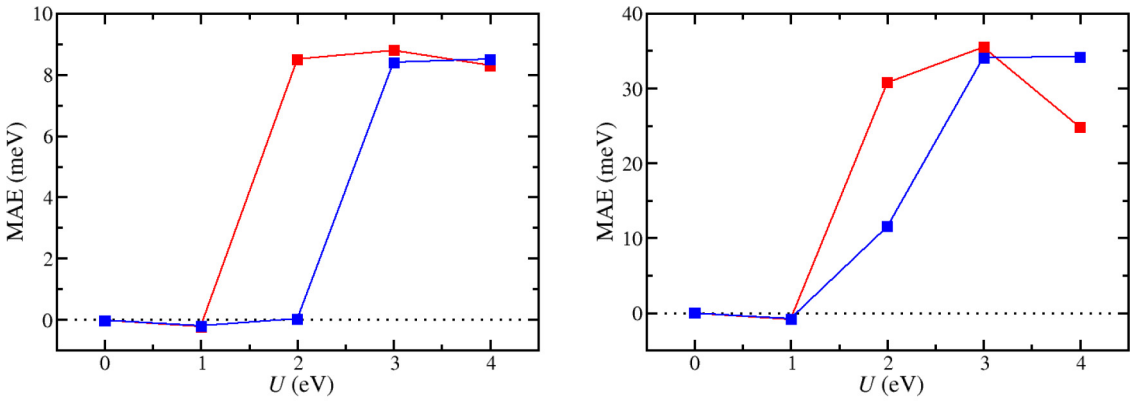

(a) Mn-MoS_2 doped ML (b) Mn-WS_2 doped ML

FIG. 4. The MAE values with respect to the values of the correlation parameter U for U-dependent (red lines) and -independent (blue lines) crystal structure of (a) Mn-MoS_2-doped ML and (b) Mn-WS_2-doped ML.

This explains the sudden increase of MAE at $U = 2$ eV when the U dependence of the crystal structure is considered. For $U > 2$ eV, a semimetallic behavior is observed for both cases. For $U = 4$ eV, the difference between the MAEs of cases I and II in the Mn-WS_2 system originates from the orbital type present at the Fermi level. Furthermore, by comparing the $3d$ energy positions in U-dependent and -independent DOS (Fig. 5), it appears that the on-site Coulomb correlation weakens the hybridization between Mn and its environment. Regarding MAE variations, the bond-length increase due to U geometrical optimization is important only when $U = 2$ eV for the two MLs and also for $U = 4$ eV in the case of Mn-WS_2-doped ML.

3. *Connection between magnetic anisotropy and orbital magnetic moments*

The relationship between magnetic anisotropy and orbital moment anisotropy (OMA) was treated by different models in order to establish a qualitative understanding of MAE origin [57,58]. The OMA is given by the difference between the in-plane orbital magnetic moment m_x and perpendicular orbital magnetic moment m_z, i.e., $\Delta m = m_x - m_z$. To reveal the relationship between MAE and OMA, the total OMA (Δm^t) and the local OMA of Mn dopant (Δm^{Mn}) as a function of U are presented in Fig. 6(a). In particular, the MAE can be related to the orbital magnetic moment through Bruno's formula [57], $\mathrm{MAE} = \frac{\xi}{4\mu_B}\Delta m^{\mathrm{Mn}}$. Here, the constant ξ stands for the SOC strength. In other words, the magnetization easy axis coincides with the direction that has the largest orbital moment [57]. For both Mn-MoS_2 and Mn-WS_2 systems, the coincidence between the magnetization easy axis and the direction of largest orbital magnetic moment is obtained for each U value. Indeed, by comparing MAE to the local OMA in Fig. 6(a), for a given U value, the easy axis and the largest orbital moment are along the same direction. Regarding the change of local OMA upon the correlation effects, the sign reversal is consistent with that of MAE. However, despite the fact that the increase of U enhances both the local OMA and MAE, their variations from $U = 2$ to 4 eV are not similar. In particular, although the $U = 3$ eV results in the largest MAE in Mn-MoS_2 and Mn-WS_2 systems, the local OMA associated with this value is not the largest among the rest of the U values.

Furthermore, the comparison between MAE and the total OMA, which includes different contributions from the Mn environment, can be also tested. To this end, the total OMA versus the Hubbard parameter U is plotted in Fig. 6(a). For the two Mn-MoS_2 and Mn-WS_2 systems, the correlation between MAE and the total OMA is shown by their sudden increase at $U = 1$ eV. Unlike MAE, there is no sign reversal of the total OMA at $U = 1$ eV in the case of Mn-WS_2-doped ML. This may due to the fact that the Bruno model is formulated for a single atom but not for structures consisting of multiple atomic species with strong hybridization and large spin-orbit interaction [58]. However, this sign reversal, consistent with MAE, occurs for Mn-MoS_2-doped ML.

Overall, the MAE's enhancement is related to the OMA's increase for both the considered doped MLs. In particular, according to Table I, the absolute values of the perpendicular orbital moment $|m_z^t|$ become considerably large when the correlation parameter increases from 0–1 to 2–4 eV. However, the in-plane orbital magnetic $|m_z^t|$ moments remain more or less constant. Therefore, the enhancement in perpendicular magnetic anisotropy is mainly due to the enhancement of the perpendicular orbital magnetic moments imposed by the on-site electron correlation.

The behavior of both MAE and OMA suggests the perpendicular orbital moment enhancement and the induced perpendicular magnetic anisotropy in the MLs have a common electronic origin. According to Refs. [47,59–61], for highly localized $3d$ orbitals including spin-orbit interaction and strong intra-atomic electron correlation, the orbital magnetic moment is anticipated to be large. In particular, this localization of the $3d$ orbitals allows atoms to retain their large atomic moments [47,59–61]. However, strong hybridization leads to the broadening of the $3d$ bands producing much smaller orbital magnetic moments [47,59–61]. Figure 3 shows the pDOS of $3d$ states of Mn dopant and d and p states of its neighboring M and X atoms, respectively, for $U = 0$ and 3 eV. In both cases, $U = 0$ and 3 eV, the high

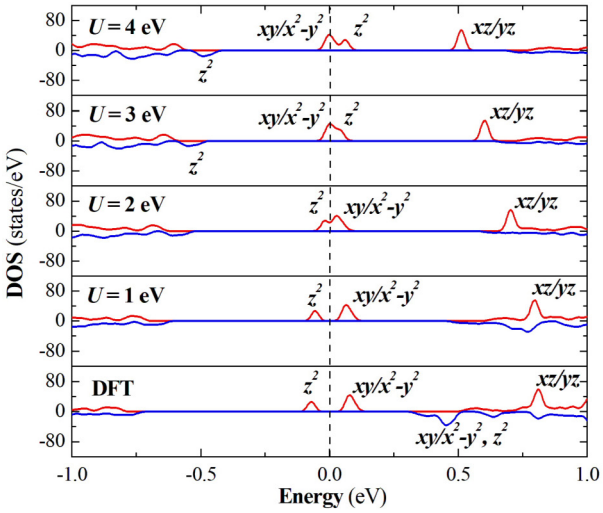

(a) Mn-doped MoS_2 ML

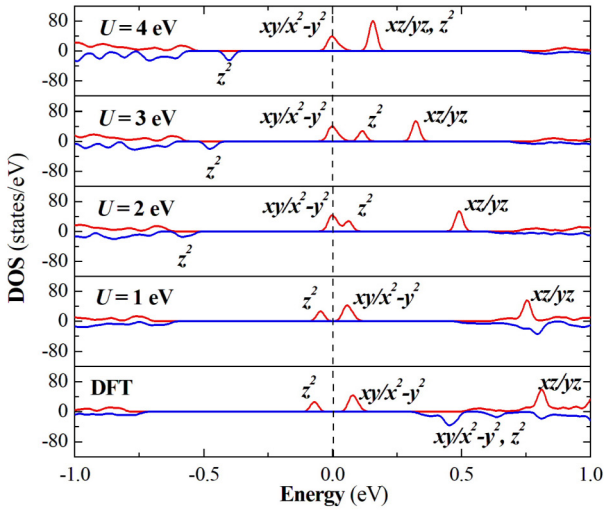

(b) Mn-doped MoS_2 ML

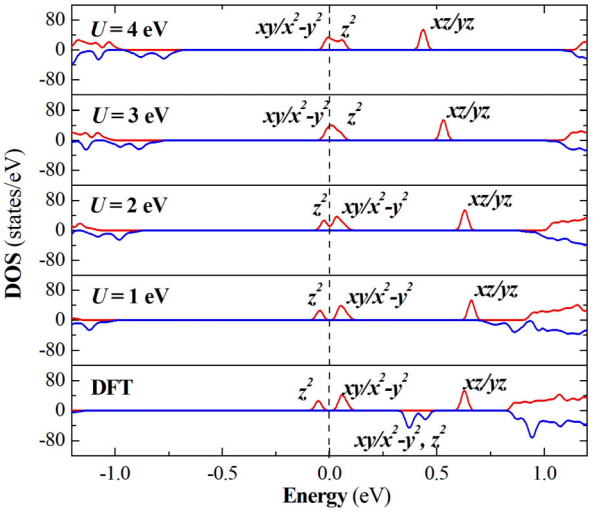

(c) Mn-doped WS_2 ML

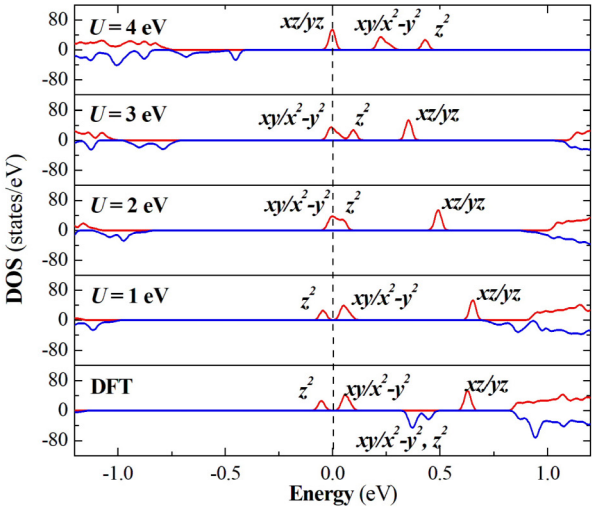

(d) Mn-doped WS_2 ML

FIG. 5. The total electronic density of states (DOS) of $U = 0$ to 4 eV for (b) U-dependent and (c) U-independent crystal structure of Mn-doped MoS_2 ML and Mn-doped WS_2 ML.

localization of Mn $3d$ states is obvious. The inclusion of U pushes the $3d$ Mn localized states towards the Fermi level which weakens the overlapping between $3d$ Mn and its neighboring $3p$ an $4d$ orbitals of M and S host atoms. This effect enlarges the orbital magnetic moments and hence the MAE.

4. Origin of magnetic anisotropy

The spin-orbit coupling is responsible for both the orbital moment and the magnetic anisotropy. The magnetization easy axis can be indicated by the competition between the second-order SOC energies per Mn dopant for in-plane (E^x_{SOC}) and out-of-plane (E^z_{SOC}) magnetization orientations, $\Delta E_{\mathrm{SOC}} = E^x_{\mathrm{SOC}} - E^z_{\mathrm{SOC}}$ [34,62], where E_{SOC} is given by the expression (2). As we can see in Fig. 6(b), the sign of ΔE_{SOC} follows that of the MAE. In particular, apart from the case of $U = 0$ and 1 eV, the out-of-plane spin-orbit energy is larger than the in-plane one which gives rise to the PMA. However, a different behavior between the variation of MAE and the variation of ΔE_{SOC} under U is obtained as depicted in Fig. 6(b). In fact, these variations of ΔE_{SOC} are similar to those of the local OMA presented in Fig. 6(a). The discrepancy between MAE and ΔE_{SOC} variations under U parameter can be understandable because a large SOC does not necessarily lead to large MAE [63].

Three principal effects behind the magnetic anisotropy are the spin-orbit effect, the crystal-field effect, and the exchange field effect [34,62]. All these effects are captured by the SOC second-order perturbation method [34] which is largely

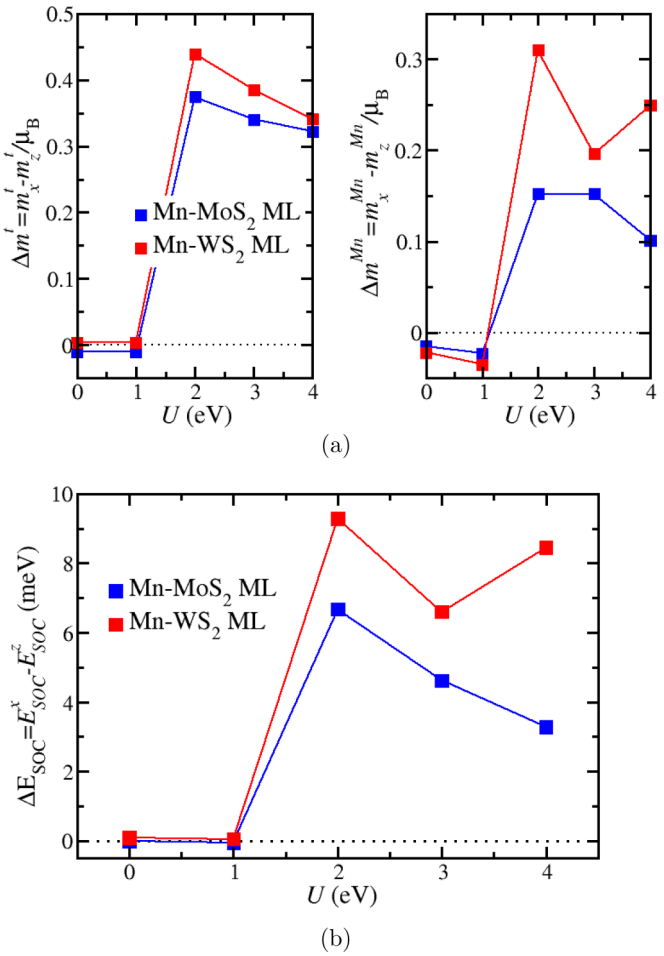

FIG. 6. (a) The total (left) and local (right) orbital magnetic anisotropy (OMA) of Mn-MS_2-doped MLs as a functions of Hubbard parameter U. (b) The spin-orbit anisotropy energy of Mn-MS_2-doped MLs as a functions of Hubbard parameter U.

adopted to investigate the MAE origin. In fact, using the crystal field and the exchange splitting of Mn 3d orbitals together with the angular momentum operators $\hat{L}_x$ and $\hat{L}_z$, the MAE can be expressed as in Ref. [34]:

$$\mathrm{MAE} \simeq \xi^2 \sum_{u^\sigma, o^{\sigma'}} \frac{|\langle u^\sigma|\hat{L}_z|o^{\sigma'}\rangle|^2 - |\langle u^\sigma|\hat{L}_x|o^{\sigma'}\rangle|^2}{\delta_{u^\sigma, o^{\sigma'}}}(2\delta_{\sigma,\sigma'} - 1). \tag{3}$$

TABLE I. The orbital magnetic moments and the atomic contributions of Mn dopant to and spin-orbit energy for in-plane and out-of-plane magnetization orientation.

	Mn-MoS_2 doped ML		Mn-MoS_2 doped ML	
U (eV)	$m_z^t(\mu_B)$	$m_x^t(\mu_B)$	$m_z^t(\mu_B)$	$m_x^t(\mu_B)$
0	−0.00	−0.01	−0.03	−0.03
1	−0.00	−0.01	−0.03	−0.02
2	−0.38	−0.01	−0.46	−0.02
3	−0.36	−0.02	−0.41	−0.03
4	−0.34	−0.02	−0.32	0.02

Here, the notations $\sigma, \sigma' = \uparrow, \downarrow$, indicate the spin directions of the occupied (o) and the unoccupied (u) states. $\delta_{u,o} = E_u - E_o$ is the energy difference between o and u states. The only nonzero matrix elements contributing to MAE are $\langle xz|\hat{L}_z|yz\rangle = 1$; $\langle xy|\hat{L}_z|x^2 - y^2\rangle = 2$; $\langle z^2|\hat{L}_x|xz, yz\rangle = \sqrt{3}$; $\langle xy|\hat{L}_x|xz, yz\rangle = 1$; and $\langle x^2 - y^2|\hat{L}_x|xz, yz\rangle = 1$. It is seen from Eq. (3) that the MAE magnitude is governed by the weight of matrix elements and the energy differences $\delta_{u,o}$. Moreover, the sign of MAE energy depends crucially on the heavy matrix element, be it with positive or negative signs. To understand the orbital origin responsible for the easy axis reversal, we consider two cases $U = 0$ and 3 eV. In particular, we analyze the pDOS of the *3d* Mn orbitals to identify the nonvanishing matrix elements that contribute negatively or positively to MAE. For $U = 0$ eV, according to Fig. 3(a) of Mn-MoS_2-doped ML and Fig. 3(c) of Mn-WS_2-doped ML, the highest occupied states are spin-up $d_{z^2}^{\uparrow}$ orbitals. According to Eq. (3), negative contribution to MAE comes from matrix elements, $\langle z^{2\uparrow}|\hat{L}_x|xz^{\uparrow}, yz^{\uparrow}\rangle$, while positive contribution corresponds to $\langle z^{2\uparrow}|\hat{L}_x|xz^{\downarrow}, yz^{\downarrow}\rangle$. Those matrix elements have similar magnitudes. Owing to the intra-atomic Hund exchange splitting (Δ_{ex}), recalling that spin-up and spin-down states with the same symmetry have different energies [4], positive contributions of $\langle z^{2\uparrow}|\hat{L}_x|xz^{\uparrow}, yz^{\uparrow}\rangle$ remain small because of the large energy denominator between the two states. Hence, the MAE is dominated by the negative contribution of $\langle z^{2\uparrow}|\hat{L}_x|xz^{\uparrow}, yz^{\uparrow}\rangle$.

For $U = 3$ eV, according to Fig. 3(b) of Mn-MoS_2-doped ML and Fig. 3(d) of Mn-WS_2-doped ML, the band of the up-spin $xy/x^2 - y^{2\uparrow}$ is half occupied. This behavior dominates both the sign and value of the MAE by favoring the PMA. According to the expression (3), the dominant contribution is positive and stems from the nonzero matrix element $\langle xy|\hat{L}_z|x^2 - y^2\rangle$ which is consistent with the DFT + U calculated MAE. However, the degeneracy of the in-plane orbitals predicts an infinite MAE which makes the second-order perturbation method unreliable in this case. In Ref. [64], it was demonstrated that when the two orbitals d_{xy} and $d_{x^2-y^2}$ are degenerate, and being at Fermi level, it favors the out-of-plane orientation magnetization. Indeed, the spin-orbit energy splitting reaches its maximum for these degenerate states when the magnetization is parallel to the z axis [64]. Therefore, the PMA originates from the spin-orbit splitting of the degenerated Mn ($d_{xy}^{\uparrow}, d_{x^2-y^2}^{\uparrow}$) orbitals placed at the Fermi level by means of the correlation effect.

Furthermore, using DFT and DFT + U, the decomposed ΔE_{SOC} on the Mn 3d orbital is presented in Fig. 7 for both Mn-MoS_2- and Mn-WS_2-doped MLs. The decomposed ΔE_{SOC} varies significantly by including the correlation effects. For the DFT case, the dominating contribution comes from the spin-orbit matrix elements involving either $d_{x^2-y^2}$ and d_{xy} orbitals. However, according to the pDOS, these coupled states are not occupied whereas only the SOC between the occupied and unoccupied states contributes to the magnetic anisotropy. The remaining large contribution comes from the coupling between d_{z^2} and d_{yz} orbitals which provides a negative contribution to ΔE_{SOC}. Therefore, the negative MAE found for $U = 0$ eV originates from the spin-orbit coupling between d_{z^2} and d_{yz} orbitals. This result is consistent with the

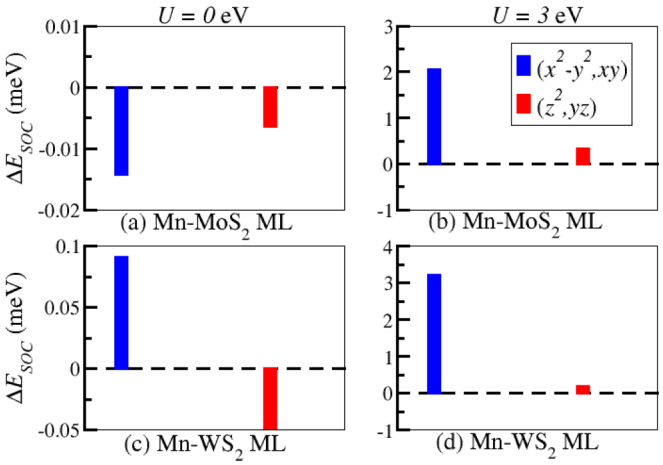

FIG. 7. The DFT (a), (c) and the DFT + U (b), (d) (U = 3 eV) difference between the in-plane and out-of-plane d-orbital projected SOC energies of Mn dopant.

second-order perturbation theory method, modeled by Eq. (3), where the matrix element $\langle z^{2\uparrow}|\hat{L}_x|xz^{\uparrow}, yz^{\uparrow}\rangle$ is found dominant. For DFT + U, an important enhancement is observed for the magnitude of spin-orbit matrix elements involving $d_{x^2-y^2}$ and d_{xy} states. These matrix elements are the major contribution to ΔE_{SOC}. Together with the semimetallic character of the in-plane orbitals, it is clear that they are behind the enhancement of MAE due to the correlations effect U.

The difference in MAE between the two MS_2 materials is related to the behavior of the in-plane orbitals under spin-orbit coupling. The DOS in Fig. 8 show that the spin-orbit splitting (δ_{SO}) of ($d_{x^2-y^2}$, d_{xy})-orbital energy is more important in the Mn WS_2 system. This explains why Mn-WS_2 has larger MAE than that of Mn-MoS_2 ML. This observation means the host TM material of Mn plays a critical role in determining the Mn induced anisotropy. In fact, for WS_2 ML, the spin-orbit coupling is stronger than for MoS_2 ML because W is heavier than Mo [44]. In particular, the upper valence band of MS_2

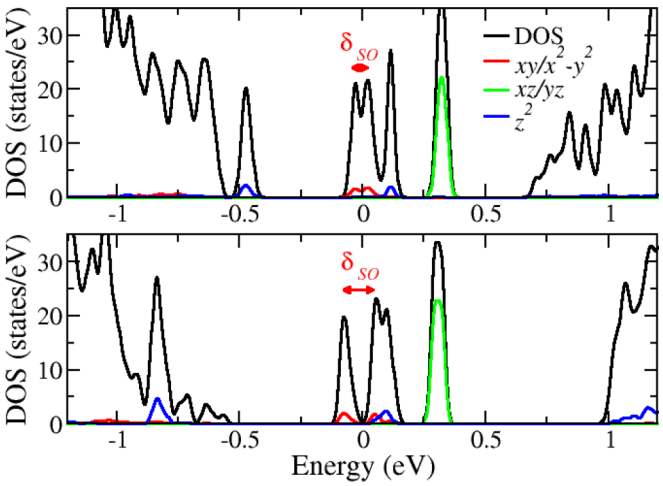

FIG. 8. The DFT + U DOS difference where the spin-orbit coupling is included for Mn-MoS_2 ML (upper panel) and Mn-WS_2 ML (down panel).

around the K point, showing strong spin-orbit splitting, is mainly composed by in-plane p-S and d-M orbitals [44]. These latter hybridize with Mn in-plane orbitals leading to a stronger spin-orbit splitting in the case of M=W.

B. Effects of Mn separation on MAE

In this section, we treat the case of Mn pairs implanted in a MoS_2 ML using a 5 × 5 × 1 supercell (see Fig. 9). Depending on Mn-Mn distance, one can generate four different doping configurations: (i) first-nearest-neighbor (nn) configuration in which the two Mn impurities are in the nn positions of the zigzag chain (1 nn-z), (ii) the 2 nn configuration in which the two Mn impurities are in the second nn positions of the armchair chain (2 nn-a), (iii) the 3 nn configuration in which the two Mn impurities are in the third nn positions of the zigzag chain (3 nn-z), and (iv) the 4 nn configuration in which the two Mn impurities are in the nn positions of the armchair chain (4 nn-a).

1. Structural stability

We study the structural stability of the different configurations through the relative energy presented in Fig. 10. The energy as a function of the Mn-Mn distance shows a behavior that differs from MoS_2 ML to WS_2 ML. In particular, for the Mn-MoS_2 system, the relative energy increases with the increase of the dopant separation distance. Hence, the doped MoS_2 structure is more stable when the Mn impurities are close to each other, i.e., the 1 nn-z case. For the Mn-WS_2 system, the relative energy does not show a monotone dependence on Mn-Mn distance. This may be due to the effect of the chain type (zigzag or armchair) on which the two dopants are placed. Same as the Mn-MoS_2 system, in Mn-WS_2-doped ML, the lower relative energy is found for the doping configuration 1 nn-z. Therefore, in both systems, Mn-MS_2 MLs, Mn impurities prefer to be in the closest substituting M sites.

2. Magnetic anisotropy

The magnetic anisotropy properties of Mn-MoS_2 and Mn-WS_2 systems are shown in Fig. 11, in which MAEs are given for all doping configurations as a function of Mn-Mn distance. For the case of the host MoS_2, MAE increases and changes its sign with the increase of Mn-Mn distance. Hence, the magnetic anisotropy goes from IMA of −1.2 meV to PMA of about 1 meV when the Mn-Mn distance increases. In particular, it is found that 1 nn-z and 2 nn-a configurations have IMA, whereas the 3 nn-z and 4 nn-a configurations correspond to PMA. For WS_2 host material, MAE remains negative for all Mn-Mn distances with a minimum of −8 meV for 1 nn-z configuration. This latter corresponds to a large in-plane magnetic anisotropy. Besides, for Mn WS_2-doped ML, MAE is not monotonically depending on Mn-Mn distance. Although the Mn-Mn distances are roughly equal in the two configurations 2 nn-a and 3 nn-z, their corresponding MAEs are different. These results suggest that the type of atomic chain has an important role in determining MAE. Thus, we can say that for zigzag or armchair configurations, MAE increases with the increase of Mn-Mn distance. Overall, by comparing the MAEs obtained here and that of the single Mn doping cases, it

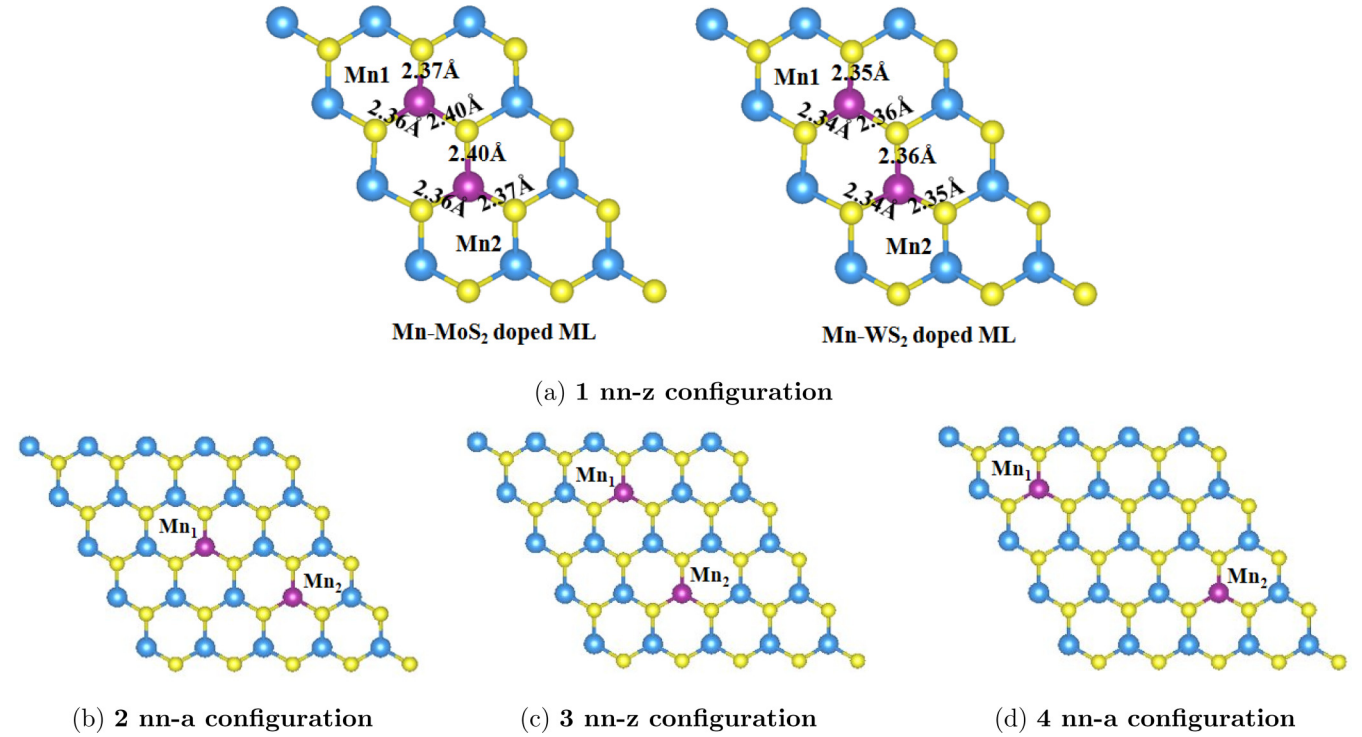

FIG. 9. Top view of the atomic structures corresponding to 8%-Mn-doped 5 × 5 × 1 MoS_2 supercells. Four doping configurations have been considered: (a) 1 nn configuration, (b) 2 nn configuration, (c) 3 nn configuration, and (d) 4 nn configuration. The yellow atoms are the sulfur (S), the blue atoms are the molybdenum (Mo), and the manganese atom is denoted by purple color.

is obvious that the diluted doping limit is required to maintain a large PMA.

3. Origin of magnetic anisotropy

In this section, as the Mn impurities atoms prefer to stay in the nearest positions at high concentrations, we choose the 1 nn-z MS_2 configurations for further study of magnetic anisotropy origin. The change of MAE in the case of the Mn-pairwise doping with respect to Mn-single doping can be related to the modification of Mn 3d states. Indeed, putting another close dopant in the structure leads to the redistribution of 3d states which is correlated with structural modifications around dopants. Therefore, we explore the structural and electronic feature changes induced by Mn pairing in the 1 nn-z MS_2 configurations. The Mn-S bond lengths are given in Fig. 9(a). In the case of single dopant, the three Mn-S bonds are equal (L) obeying the D_{3h} symmetry. Contrary to the case of single dopant, which obeys the D_{3h} symmetry, the lengths are no longer equal, indicating a symmetry reduction. The lengths of Mn_1-S and Mn_2-S bonds that relate the two Mn

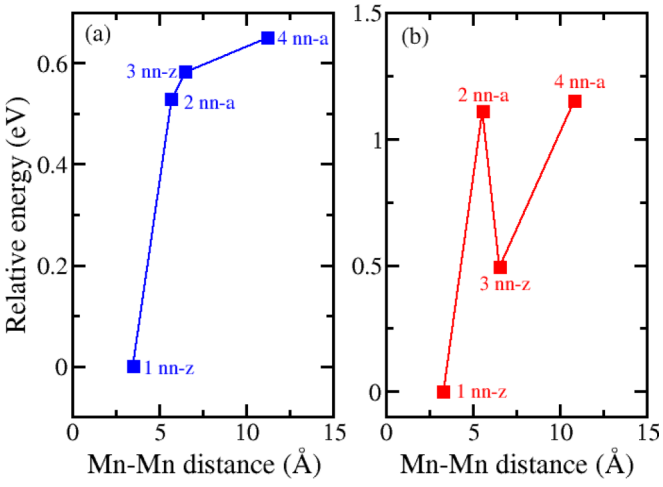

FIG. 10. Mn-Mn distance dependence of relative energy of Mn pair doped (a) MoS_2 ML and (b) WS_2 ML.

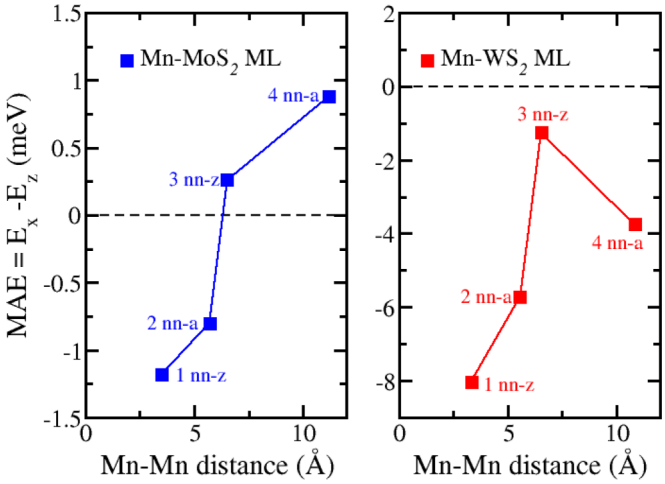

FIG. 11. Mn-Mn distance dependence of (a) magnetic anisotropy energy and (b) the orbital magnetic anisotropy Δm_0 values for Mn-doped MoS_2.

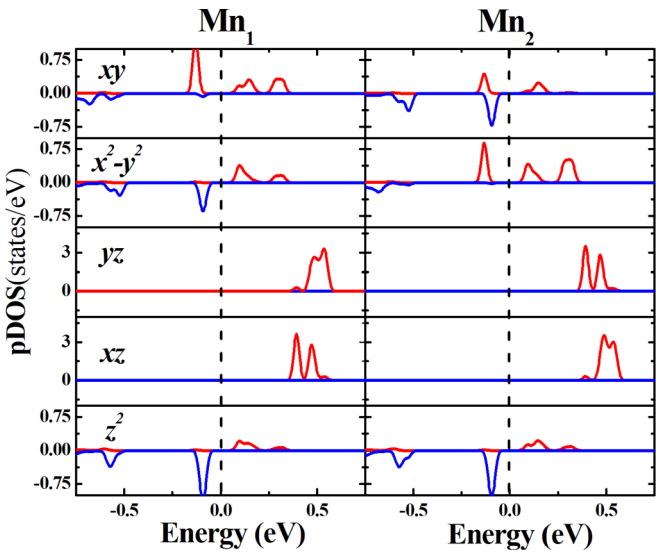

(a) Mn MoS_2 ML

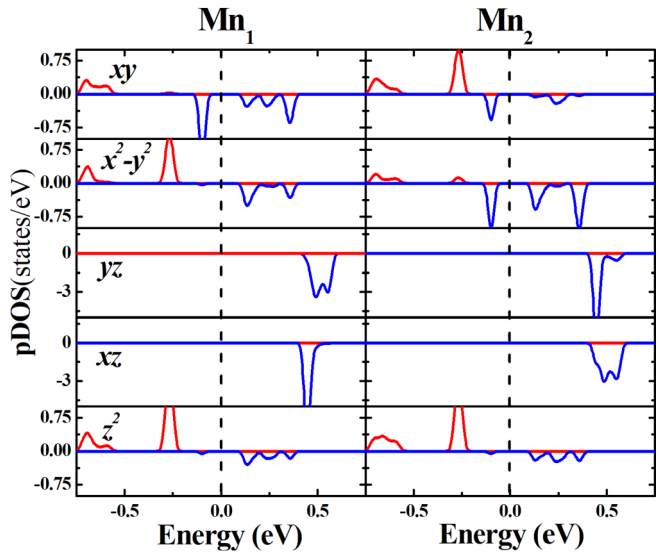

(b) Mn WS_2 ML

FIG. 12. The projected electron density of states of Mn_1 and Mn_2 d orbitals in (a) MoS_2 ML and (b) WS_2 ML. The red and blue lines denote spin-up and spin-down channels, respectively. The Fermi level is indicated by the black dashed line.

atoms are the largest lengths. This means that the two Mn dopants repel each other. In the meantime, the distances of Mn_1-S and Mn_2-S bonds, that relate each Mn atom to the nearest M of the zigzag chain, are the lowest lengths. To analyze the electronic structure, the pDOS are plotted in Figs. 12(a) and 12(b). According to Figs. 12(a) and 12(b), placing the second Mn atom in a metal site close to the first one induces electronic structure modifications. Considering in-plane orbitals, their degeneracy is lifted as shown in Figs. 12(a) and 12(b). In fact, the Mn_1 d_{xy} orbital is coupled to the Mn_2 $d_{x^2-y^2}$ orbital as they are pointed toward each other because of the hexagonal geometry. The remaining Mn_1 $d_{x^2-y^2}$ and Mn_2 d_{xy} orbitals are mostly coupled to the d orbital of the surrounding TM host atoms and they show slightly different behaviors compared to each other. A quite similar effect is shown by out-of-plane orbitals (d_{xz}, d_{yz}) where their associated degeneracy is lifted, as it can be seen in Figs. 12(a) and 12(b). In particular, the Mn_1 d_{yz} and Mn_2 d_{xz} orbital hybridize with the same $3p$ of the S cation while the Mn_1 d_{xz} and Mn_2 d_{yz} orbitals are coupled to the S atom with the Mo or W environment.

We now discuss the MAE origin of Mn-MoS_2-doped ML, upon Mn pairing. According to Fig. 12(a), the occupied states correspond to the orbitals d_{xy}, $d_{x^2-y^2}$, and d_{z^2}, while the unoccupied states correspond to d_{xy}, $d_{x^2-y^2}$, d_{xz}, and d_{yz}. For the Mn_1 case, the prominent coupling elements are $\langle xy^{\uparrow}|\hat{L}_z|xz, yz^{\uparrow}\rangle$ and $\langle z^{2\downarrow}|\hat{L}_z|xz, yz^{\uparrow}\rangle$. In particular, for Mn_2, the prominent coupling elements are $\langle x^2-y^{2\uparrow}|\hat{L}_z|xz, yz^{\uparrow}\rangle$ and $\langle z^{2\downarrow}|\hat{L}_z|xz, yz^{\uparrow}\rangle$. Here, $\langle xy^{\uparrow}|\hat{L}_z|xz, yz^{\uparrow}\rangle$ gives a positive contribution to MAE while $\langle z^{2\downarrow}|\hat{L}_z|xz, yz^{\uparrow}\rangle$ gives a negative contribution. Because of the dominance of $\langle x^2-y^{2\uparrow}|\hat{L}_z|xz, yz^{\uparrow}\rangle$ and $\langle xy^{\uparrow}|\hat{L}_z|xz, yz^{\uparrow}\rangle$, the 1 nn-z configuration of Mn-MoS_2 ML prefers IMA. In the case of Mn-MoS_2-doped ML, the matrix elements involving minority-spin $d^{\downarrow}_{xy}$, $d^{\downarrow}_{x^2-y^2}$, $d^{\downarrow}_{xz}$, and $d^{\downarrow}_{yz}$ states yield positive contributions to MAE. In particular, for Mn_1, the positive contribution comes from $\langle xy^{\downarrow}|\hat{L}_z|xy, x^2-y^{2\downarrow}\rangle$ and $\langle xy^{\downarrow}|\hat{L}_z|xz, yz^{\downarrow}\rangle$. Besides, for Mn_1, the positive contribution comes from $\langle x^2-y^{2\downarrow}|\hat{L}_z|xy, x^2-y^{2\downarrow}\rangle$ and $\langle x^2-y^{2\downarrow}|\hat{L}_z|xz, yz^{\downarrow}\rangle$. All these positive contributions finally lead to IMA for the 1 nn-z configuration of Mn-WS_2 ML.

IV. CONCLUSION

By performing DFT + U calculations, we have investigated the magnetic anisotropy induced by Mn doping in MoS_2 and WS_2 MLs. In the case of a well-isolated Mn atom substituting a W center, a large positive MAE of 35 meV is obtained for Mn-WS_2-doped ML. For Mn-MoS_2-doped ML a smaller MAE of 8 meV is found. These results mean that the preferential direction of magnetization is perpendicular to the ML plane when the origin of large MAE is attributed to the presence of in-plane Mn orbitals located in the vicinity of the Fermi level. In the case of the Mn pairwise doping, a spin reorientation transition from out-of-plane to in-plane magnetization takes place when the Mn-Mn distance decreases. In general, it is apparent that the clustering of Mn dopants favors the in-plane magnetization. Our findings show that important magnetic anisotropy can be found in Mn-doped WS_2 and MoS_2 ML only for considerable Mn-Mn distances.

ACKNOWLEDGMENTS

S.L. acknowledges funding from the Priority Programme SPP 2244 2D Materials—Physics of van der Waals Heterostructures of the Deutsche Forschungsgemeinschaft (Project No. LO 1659/7-1) and the European Research Council (ERC) under the European Union's Horizon 2020 research and innovation program (ERC consolidator Grant No. 681405 DYNASORE). I.C.G. thanks the CALMIP initiative for the generous allocation of computational time, through Project No. p0812, as well as GENCI-CINES and GENCI-IDRIS for Grant No. A008096649.

[1] K. Zhang, S. Feng, J. Wang, A. Azcatl, N. Lu, R. Addou, N. Wang, C. Zhou, J. Lerach, V. Bojan *et al.*, Nano Lett. **15**, 6586 (2015).

[2] J. Wang, F. Sun, S. Yang, Y. Li, C. Zhao, M. Xu, Y. Zhang, and H. Zeng, Appl. Phys. Lett. **109**, 092401 (2016).

[3] Y. C. Cheng, Z. Y. Zhu, W. B. Mi, Z. B. Guo, and U. Schwingenschlögl, Phys. Rev. B **87**, 100401(R) (2013).

[4] R. Mishra, W. Zhou, S. J. Pennycook, S. T. Pantelides, and J.-C. Idrobo, Phys. Rev. B **88**, 144409 (2013).

[5] A. Ramasubramaniam and D. Naveh, Phys. Rev. B **87**, 195201 (2013).

[6] Q. Yue, S. Chang, S. Qin, and J. Li, Phys. Lett. A **377**, 1362 (2013).

[7] W. Cong, Z. Tang, X. Zhao, and J. Chu, Sci. Rep. **5**, 9361 (2015).

[8] X.-L. Fan, Y.-R. An, and W.-J. Guo, Nanoscale Res. Lett. **11**, 154 (2016).

[9] Q. Fang, X. Zhao, Y. Huang, K. Xu, T. Min, P. K. Chu, and F. Ma, Phys. Chem. Chem. Phys. **20**, 553 (2018).

[10] J. Gao, Y. D. Kim, L. Liang, J. C. Idrobo, P. Chow, J. Tan, B. Li, L. Li, B. G. Sumpter, T.-M. Lu *et al.*, Adv. Mater. **28**, 9735 (2016).

[11] L. Sun, W. Zhou, Y. Liang, L. Liu, and P. Wu, Comput. Mater. Sci. **117**, 489 (2016).

[12] L. Seixas, A. Carvalho, and A. H. Castro Neto, Phys. Rev. B **91**, 155138 (2015).

[13] D. Odkhuu, Phys. Rev. B **94**, 060403(R) (2016).

[14] D. Odkhuu, S. H. Rhim, N. Park, and S. C. Hong, Phys. Rev. B **88**, 184405 (2013).

[15] Y. Song, X. Wang, and W. Mi, Phys. Rev. Materials **1**, 074408 (2017).

[16] Y.-X. Song, W.-Y. Tong, Y.-H. Shen, S.-J. Gong, Z. Tang, and C.-G. Duan, J. Phys. Condens. Matter **29**, 475803 (2017).

[17] B. Zhu, X. Chen, and X. Cui, Sci. Rep. **5**, 9218 (2015).

[18] D. W. Kidd, D. K. Zhang, and K. Varga, Phys. Rev. B **93**, 125423 (2016).

[19] I. Kylänpää and H.-P. Komsa, Phys. Rev. B **92**, 205418 (2015).

[20] A. Raja, A. Chaves, J. Yu, G. Arefe, H. M. Hill, A. F. Rigosi, T. C. Berkelbach, P. Nagler, C. Schüller, T. Korn *et al.*, Nat. Commun. **8**, 15251 (2017).

[21] A. V. Stier, N. P. Wilson, G. Clark, X. Xu, and S. A. Crooker, Nano Lett. **16**, 7054 (2016).

[22] R. Sundaram, M. Engel, A. Lombardo, R. Krupke, A. Ferrari, P. Avouris, and M. Steiner, Nano Lett. **13**, 1416 (2013).

[23] Y. Ye, Z. Ye, M. Gharghi, H. Zhu, M. Zhao, Y. Wang, X. Yin, and X. Zhang, Appl. Phys. Lett. **104**, 193508 (2014).

[24] Y. Ye, Z. J. Wong, X. Lu, X. Ni, H. Zhu, X. Chen, Y. Wang, and X. Zhang, Nat. Photonics **9**, 733 (2015).

[25] Y. Cai, G. Zhang, and Y.-W. Zhang, J. Am. Chem. Soc. **136**, 6269 (2014).

[26] B. W. Baugher, H. O. Churchill, Y. Yang, and P. Jarillo-Herrero, Nano Lett. **13**, 4212 (2013).

[27] D. Lembke and A. Kis, ACS Nano **6**, 10070 (2012).

[28] H. Schmidt, S. Wang, L. Chu, M. Toh, R. Kumar, W. Zhao, A. H. Castro Neto, J. Martin, S. Adam, B. Özyilmaz *et al.*, Nano Lett. **14**, 1909 (2014).

[29] B. Radisavljevic, M. B. Whitwick, and A. Kis, ACS Nano **5**, 9934 (2011).

[30] Y. Zhang, J. Ye, Y. Matsuhashi, and Y. Iwasa, Nano Lett. **12**, 1136 (2012).

[31] J. Lin, J. Zhong, S. Zhong, H. Li, H. Zhang, and W. Chen, Appl. Phys. Lett. **103**, 063109 (2013).

[32] A. A. Khajetoorians and J. Wiebe, Science **344**, 976 (2014).

[33] C.-G. Duan, J. P. Velev, R. F. Sabirianov, Z. Zhu, J. Chu, S. S. Jaswal, and E. Y. Tsymbal, Phys. Rev. Lett. **101**, 137201 (2008).

[34] D.-s. Wang, R. Wu, and A. J. Freeman, Phys. Rev. B **47**, 14932 (1993).

[35] J. Ibanez-Azpiroz, M. dos Santos Dias, S. Blügel, and S. Lounis, Nano Lett. **16**, 4305 (2016).

[36] I. G. Rau, S. Baumann, S. Rusponi, F. Donati, S. Stepanow, L. Gragnaniello, J. Dreiser, C. Piamonteze, F. Nolting, S. Gangopadhyay *et al.*, Science **344**, 988 (2014).

[37] F. Donati, S. Rusponi, S. Stepanow, C. Wäckerlin, A. Singha, L. Persichetti, R. Baltic, K. Diller, F. Patthey, E. Fernandes *et al.*, Science **352**, 318 (2016).

[38] Y. Yue, C. Jiang, Y. Han, M. Wang, J. Ren, and Y. Wu, J. Magn. Magn. Mater. **496**, 165929 (2020).

[39] W.-F. Li, C. Fang, and M. A. van Huis, Phys. Rev. B **94**, 195425 (2016).

[40] G.-B. Liu, W.-Y. Shan, Y. Yao, W. Yao, and D. Xiao, Phys. Rev. B **88**, 085433 (2013).

[41] E. S. Kadantsev and P. Hawrylak, Solid State Commun. **152**, 909 (2012).

[42] S. Lebègue and O. Eriksson, Phys. Rev. B **79**, 115409 (2009).

[43] M. Khan and M. N. Leuenberger, J. Phys. Condens. Matter **30**, 155802 (2018).

[44] Z. Y. Zhu, Y. C. Cheng, and U. Schwingenschlögl, Phys. Rev. B **84**, 153402 (2011).

[45] D. S. Parker, N. Ghimire, J. Singleton, J. D. Thompson, E. D. Bauer, R. Baumbach, D. Mandrus, L. Li, and D. J. Singh, Phys. Rev. B **91**, 174401 (2015).

[46] I. Yang, S. Y. Savrasov, and G. Kotliar, Phys. Rev. Lett. **87**, 216405 (2001).

[47] J. Klatyk, W. Schnelle, F. R. Wagner, R. Niewa, P. Novák, R. Kniep, M. Waldeck, V. Ksenofontov, and P. Gütlich, Phys. Rev. Lett. **88**, 207202 (2002).

[48] G. Kresse and J. Hafner, Phys. Rev. B **47**, 558 (1993).

[49] G. Kresse and J. Hafner, Phys. Rev. B **49**, 14251 (1994).

[50] P. E. Blöchl, Phys. Rev. B **50**, 17953 (1994).

[51] G. Kresse and D. Joubert, Phys. Rev. B **59**, 1758 (1999).

[52] J. P. Perdew, K. Burke, and M. Ernzerhof, Phys. Rev. Lett. **77**, 3865 (1996).

[53] S. L. Dudarev, G. A. Botton, S. Y. Savrasov, C. J. Humphreys, and A. P. Sutton, Phys. Rev. B **57**, 1505 (1998).

[54] P. E. Blöchl, O. Jepsen, and O. K. Andersen, Phys. Rev. B **49**, 16223 (1994).

[55] D. Koelling and B. Harmon, J. Phys. C **10**, 3107 (1977).

[56] J. Hafner, J. Comp. Chem. **29**, 2044 (2008).

[57] P. Bruno, Phys. Rev. B **39**, 865 (1989).

[58] C. Andersson, B. Sanyal, O. Eriksson, L. Nordström, O. Karis, D. Arvanitis, T. Konishi, E. Holub-Krappe, and J. H. Dunn, Phys. Rev. Lett. **99**, 177207 (2007).

[59] S. K. Kwon and B. I. Min, Phys. Rev. Lett. **84**, 3970 (2000).

[60] K. Pradhan, P. Sen, J. U. Reveles, and S. N. Khanna, J. Phys. Condens. Matter **20**, 255243 (2008).

[61] D. J. Huang, C. F. Chang, H.-T. Jeng, G. Y. Guo, H.-J. Lin, W. B. Wu, H. C. Ku, A. Fujimori, Y. Takahashi, and C. T. Chen, Phys. Rev. Lett. **93**, 077204 (2004).

[62] D. Odkhuu and N. Kioussis, Phys. Rev. B **97**, 094404 (2018).

[63] R. Skomski, A. Kashyap, and A. Enders, J. Appl. Phys. **109**, 07E143 (2011).

[64] G. H. O. Daalderop, P. J. Kelly, and M. F. H. Schuurmans, Phys. Rev. B **50**, 9989 (1994).